Helium-3 microscopic optical model potential based on the Skyrme interaction

Hairui Guo,* Yue Zhang, Yinlu Han, and Qingbiao Shen
China Institute of Atomic Energy, P. O. Box 275(41), Beijing 102413, People's Republic of China
(Received 13 January 2009; revised manuscript received 8 April 2009; published 9 June 2009)

A microscopic helium-3 optical potential is obtained by Green function method through nuclear matter approximation and local density approximation based on the effective Skyrme interaction. The reaction cross sections and the elastic scattering angular distributions are calculated by the microscopic optical potential for nuclides in the mass range $12 \leqslant A \leqslant 208$ with incident helium-3 energies from threshold up to 200 MeV. The results of theoretical calculations are compared with the experimental data.

DOI: 10.1103/PhysRevC.79.064601 PACS number(s): 24.10.Ht, 25.55.−e, 24.10.Cn

I. INTRODUCTION

The optical model is one of the most fundamental theoretical models in nuclear reaction theory. It is applied widely in the nuclear reaction calculations (the calculations of total, nonelastic, elastic cross sections, and elastic-scattering angular distributions, and the transmission coefficient of the compound nucleus and the preequilibrium emission process, and so on). The key point of the optical model is the optical model potential. The phenomenological optical potential includes many adjustable parameters, and it is obtained by adjusting its parameters to fit the existing experimental data, so it cannot predict the unknown data with certainty. The microscopic optical potential (MOP) is derived theoretically based on the nucleon-nucleon interaction (not the existing experimental data). It has no free parameters and is usually applicable in a wide range of mass number and energy. Thus, the derivation of the microscopic optical potential is one of the most important problems in nuclear theory and is of both theoretical and practical interest.

At present, there are some microscopic optical potentials [1–3] for nucleon and deuteron based on nucleon-nucleon interaction, and they can reproduce the experimental data quite well. For ^{3}He, despite there are some optical potentials constructed from phenomenological approach [4–6] and some optical potentials constructed from a combined microscopic and phenomenological approach [7,8], there is no optical potential for ^{3}He obtained from a microscopic approach yet. Samaddar [7] and Sinha [8] developed the optical potentials for ^{3}He in terms of the optical potentials of its constituent nucleons, however, both optical potentials are still obtained by adjusting parameters based on existing experimental data like phenomenological optical potentials in the end, and they cannot reproduce the experimental data satisfactorily. In the present paper we generate a microscopic optical potential for ^{3}He without free parameters based on Skyrme nucleon-nucleon interaction.

In view of the many-body theory, the nucleon optical potential is identified with the mass operator of the one-particle Green function [9], which makes it possible to utilize the mass operator to get the nucleon microscopic optical potential. In Refs. [1,2], the nucleon microscopic optical potentials are obtained by Green function method through nuclear matter approximation and local density approximation based on some Skyrme interactions, and it is shown that the results calculated by the nucleon microscopic optical potentials are comparable to that calculated by phenomenological ones in fitting the empirical data. Encouraged by the success of the nucleon microscopic optical potential, the helium-3 microscopic optical potential is given from the three-particle Green function based on Skyrme interaction in this paper, and the nuclear matter approximation and local density approximation are used. The first-order and the imaginary part of second-order mass operators of the three-particle Green function denote the real and imaginary parts of the helium-3 microscopic optical potential, respectively. The helium-3 microscopic optical potential obtained is used to calculated the reaction cross sections and the elastic scattering angular distributions in the mass range $12 \leqslant A \leqslant 208$ with incident helium-3 energies from threshold up to 200 MeV, and the calculated results are compared with experimental data.

In Sec. II, the general formulation of the MOP for ^{3}He is presented. The calculated results and analysis are given in Sec. III. Finally, in Sec. IV a summary is given.

II. THEORETICAL MODEL

The Hamiltonian of the system composed of the incident particle and the target nucleus, which only considers the two-body interaction, can be expressed as

$$H = H_0 + H_1, \tag{1}$$

where

$$H_0 = \sum_i (t_i + U_i), \tag{2}$$

$$H_1 = \frac{1}{2}\sum_{i\neq j} V_{ij} - \sum_i U_i \tag{3}$$

with H_0 being the single-particle Hamiltonian, H_1 being the residual interaction, and U_i being the single-particle mean field.

* ghr@ciae.ac.cn

The three-particle Green function is expressed as

$$iG(\alpha_1\alpha_2\alpha_3, \beta_1\beta_2\beta_3; t_1 - t_2) = \frac{\langle\phi_0|T\left[U_\eta(\infty, -\infty)\xi_{\alpha_3}(t_1)\xi_{\alpha_2}(t_1)\xi_{\alpha_1}(t_1)\xi^+_{\beta_1}(t_2)\xi^+_{\beta_2}(t_2)\xi^+_{\beta_3}(t_2)\right]|\phi_0\rangle}{\langle\phi_0|U_\eta(-\infty, +\infty)|\phi_0\rangle}$$
$$= \langle\phi_0|T\left[U_\eta(-\infty, +\infty)\xi_{\alpha_3}(t_1)\xi_{\alpha_2}(t_1)\xi_{\alpha_1}(t_1)\xi^+_{\beta_1}(t_2)\xi^+_{\beta_2}(t_2)\xi^+_{\beta_3}(t_2)\right]|\phi_0\rangle_L, \quad (4)$$

where $|\phi_0\rangle$ is the eigenstate of H_0, T is the time-ordering symbol, ξ_{α_1}, ξ_{α_2}, and ξ_{α_3} are the annihilation operators in interaction representation, $\xi^+_{\beta_1}$, $\xi^+_{\beta_2}$, and $\xi^+_{\beta_3}$ are the creation operators in interaction representation, L denotes that only the linked diagrams are reserved. $U_\eta(\infty, -\infty)$ is the time-evolution operator expressed as

$$U_\eta(\infty, -\infty) = \sum_{n=0}^{\infty}\left(\frac{-i}{\hbar}\right)^n \frac{1}{n!}\int d\tau_1 \int d\tau_2 \cdots\cdots$$
$$\times \int d\tau_n \exp[-\eta(|\tau_1| + |\tau_2| + \cdots\cdots + |\tau_n|)]$$
$$\times T\{H_1(\tau_1)H_1(\tau_2)\cdots\cdots H_1(\tau_n)\}, \quad (5)$$

where η is the infinitesimal imported in adiabatic approximation.

The three-particle Green function satisfies the Dyson equation

$$iG(\alpha_1\alpha_2\alpha_3, \beta_1\beta_2\beta_3; \omega)$$
$$= iG^{(0)}(\alpha_1\alpha_2\alpha_3, \beta_1\beta_2\beta_3; \omega)$$
$$+ \frac{i}{\hbar}\sum_{\rho\lambda\theta\mu\nu\delta} iG^{(0)}(\alpha_1\alpha_2\alpha_3, \rho\lambda\theta; \omega)[U_{\rho\lambda\theta,\mu\nu\delta}$$
$$- M(\rho\lambda\theta, \mu\nu\delta; \omega)]iG(\mu\nu\delta, \beta_1\beta_2\beta_3; \omega), \quad (6)$$

where $U_{\rho\lambda\theta,\mu\nu\delta}$ is mean field, and $M(\rho\lambda\theta, \mu\nu\delta)$ is the mass operator which can be expanded into

$$M(\rho\lambda\theta, \mu\nu\delta; \omega) = M^{(1)}(\rho\lambda\theta, \mu\nu\delta; \omega)$$
$$+ M^{(2)}(\rho\lambda\theta, \mu\nu\delta; \omega) + \cdots. \quad (7)$$

For the scattering process, the mass operator $M(\alpha_1\alpha_2\alpha_3, \alpha_1\alpha_2\alpha_3; \omega)$ is identified with the microscopic optical potential for ^{3}He.

The three-particle Green function can be expanded into perturbation series:

$$iG(\alpha_1\alpha_2\alpha_3, \beta_1\beta_2\beta_3; t_1 - t_2)$$
$$= iG^{(0)}(\alpha_1\alpha_2\alpha_3, \beta_1\beta_2\beta_3; t_1 - t_2)$$
$$+ iG^{(1)}(\alpha_1\alpha_2\alpha_3, \beta_1\beta_2\beta_3; t_1 - t_2)$$
$$+ iG^{(2)}(\alpha_1\alpha_2\alpha_3, \beta_1\beta_2\beta_3; t_1 - t_2) + \cdots. \quad (8)$$

As the contribution of the higher-order terms is quite small, it is considered only up to the second order in this paper. The corresponding Feynman diagrams include one zeroth-order diagram, nine first-order diagrams given in Fig. 1, and 96 second-order diagrams.

As studying the helium-3 optical potential, ^{3}He is considered as a cluster and the nucleon-nucleon direct interactions in ^{3}He are not considered. Since the three Feynman diagrams in Fig. 1(b) describe the direct interactions of the three nucleons in ^{3}He, only the Feynman diagrams in Fig. 1(a) contribute to the first-order term of the three-particle Green function. By performing the Fourier transformation, the first-order term of the three-particle Green function can be expressed as

$$iG^{(1)}(\alpha_1\alpha_2, \beta_1\beta_2; \omega)$$
$$= \frac{i}{\hbar} iG^{(0)}_{\alpha_1\alpha_2\alpha_3}(\omega)\left[U_{\alpha_1\beta_1} - \sum_\rho V_{\alpha_1\rho,\beta_1\rho}n_\rho\right]$$
$$\times iG^{(0)}_{\beta_1\alpha_2\alpha_3}(\omega)\delta_{\alpha_2\beta_2}\delta_{\alpha_3\beta_3}$$
$$+ \frac{i}{\hbar}\delta_{\alpha_1\beta_1}\delta_{\alpha_3\beta_3} iG^{(0)}_{\alpha_1\alpha_2\alpha_3}(\omega)\left[U_{\alpha_2\beta_2} - \sum_\rho V_{\alpha_2\rho,\beta_2\rho}n_\rho\right]$$
$$\times iG^{(0)}_{\alpha_1\beta_2\alpha_3}(\omega)$$
$$+ \frac{i}{\hbar}\delta_{\alpha_1\beta_1}\delta_{\alpha_2\beta_2} iG^{(0)}_{\alpha_1\alpha_2\alpha_3}(\omega)\left[U_{\alpha_3\beta_3} - \sum_\rho V_{\alpha_3\rho,\beta_3\rho}n_\rho\right]$$
$$\times iG^{(0)}_{\alpha_1\alpha_2\beta_3}(\omega), \quad (9)$$

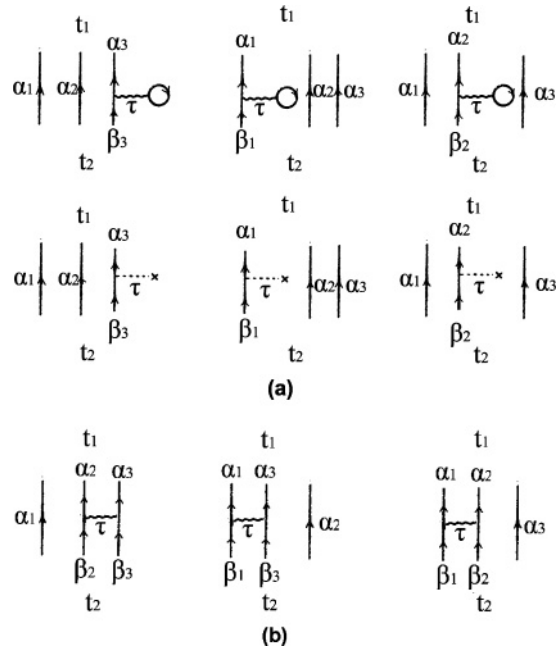

FIG. 1. First-order diagrams of the three-particle Green function.

where

$$n_\rho = \begin{cases} 1, & \text{below the Fermi surface} \\ 0, & \text{above the Fermi surface,} \end{cases} \tag{10}$$

$$V_{\alpha\rho,\beta\rho} = \langle \alpha\rho | V | \beta\rho \rangle_A, \tag{11}$$

where A denotes antisymmetrization and V is the two-body nucleon-nucleon interaction.

From the Dyson equation, the first-order term of the three-particle Green function can be also expressed as

$$\begin{aligned} & iG^{(1)}(\alpha_1\alpha_2\alpha_3, \beta_1\beta_2\beta_3; \omega) \\ & = \frac{i}{\hbar} iG^{(0)}_{\alpha_1\alpha_2\alpha_3}(\omega) \big[U_{\alpha_1\alpha_2\alpha_3,\beta_1\beta_2\beta_3} \\ & \quad - M^{(1)}(\alpha_1\alpha_2\alpha_3, \beta_1\beta_2\beta_3) \big] iG^{(0)}_{\beta_1\beta_2\beta_3}(\omega). \end{aligned} \tag{12}$$

The Hartree-Fock mean field $U_{\alpha_1\alpha_2\alpha_3}$ is expressed as

$$U_{\alpha_1\alpha_2\alpha_3} = M^{(1)}_{\alpha_1\alpha_2\alpha_3} \tag{13}$$

so $M^{(1)}_{\alpha_1\alpha_2\alpha_3}$ gives the real part of the MOP for ^{3}He. By comparing Eqs. (9) and (12), it can be obtained:

$$U_{\alpha_1\alpha_2\alpha_3} = U_{\alpha_1} + U_{\alpha_2} + U_{\alpha_3}, \tag{14}$$

$$M^{(1)}_{\alpha_1\alpha_2\alpha_3} = \sum_\rho V_{\alpha_1\rho,\alpha_1\rho} n_\rho + \sum_\rho V_{\alpha_2\rho,\alpha_2\rho} n_\rho + \sum_\rho V_{\alpha_3\rho,\alpha_3\rho} n_\rho. \tag{15}$$

In the right-hand side of Eq. (15), each term is just the contribution of the real part of the microscopic optical potential for each nucleon [1,2] in ^{3}He.

Under the mean field approximation, 78 of the second-order Feynman diagrams can be offset. The residual second-order Feynman diagrams are given in Fig. 2. The Feynman diagrams in Fig. 2(b) describe the direct interactions among the three nucleons in ^{3}He, and the Feynman diagrams in Fig. 2(c) describe the indirect interactions which can make helium-3 breakup, so the Feynman diagrams in Fig. 2(b) and 2(c) can be ignored. Only the Feynman diagrams in Fig. 2(a) contribute to the second-order term of the three-particle Green function.

By performing Fourier transformation, the second-order term of the three-particle Green function can be expressed as

$$\begin{aligned} & iG^{(2)}(\alpha_1\alpha_2\alpha_3, \beta_1\beta_2\beta_3; \omega) \\ & = -\delta_{\alpha_1\beta_1}\delta_{\alpha_3\beta_3} iG^{(0)}_{\alpha_1\alpha_2\alpha_3}(\omega) \frac{i}{\hbar} \left[\frac{1}{2} \sum_{\rho\delta\lambda} \frac{V_{\alpha_2\lambda,\delta\rho} V_{\delta\rho,\beta_2\lambda}}{\omega - \varepsilon_{\alpha_1} - \varepsilon_{\alpha_3} - \varepsilon_\rho - \varepsilon_\delta + \varepsilon_\lambda + i\eta} n_\lambda (1-n_\delta)(1-n_\rho) \right] iG^{(0)}_{\alpha_1\beta_2\alpha_3}(\omega) \\ & \quad - iG^{(0)}_{\alpha_1\alpha_2\alpha_3}(\omega) \frac{i}{\hbar} \left[\frac{1}{2} \sum_{\rho\delta\lambda} \frac{V_{\alpha_1\lambda,\delta\rho} V_{\delta\rho,\beta_1\lambda}}{\omega - \varepsilon_{\alpha_2} - \varepsilon_{\alpha_3} - \varepsilon_\rho - \varepsilon_\delta + \varepsilon_\lambda + i\eta} n_\lambda (1-n_\delta)(1-n_\rho) \right] iG^{(0)}_{\beta_1\alpha_2\alpha_3}(\omega) \delta_{\alpha_2\beta_2}\delta_{\alpha_3\beta_3} \\ & \quad - \delta_{\alpha_1\beta_1}\delta_{\alpha_2\beta_2} iG^{(0)}_{\alpha_1\alpha_2\alpha_3}(\omega) \frac{i}{\hbar} \left[\frac{1}{2} \sum_{\rho\delta\lambda} \frac{V_{\alpha_3\lambda,\delta\rho} V_{\delta\rho,\beta_3\lambda}}{\omega - \varepsilon_{\alpha_1} - \varepsilon_{\alpha_2} - \varepsilon_\rho - \varepsilon_\delta + \varepsilon_\lambda + i\eta} n_\lambda (1-n_\delta)(1-n_\rho) \right] iG^{(0)}_{\alpha_1\alpha_2\beta_3}(\omega), \end{aligned} \tag{16}$$

where

$$\omega = \varepsilon_{\alpha_1} + \varepsilon_{\alpha_2} + \varepsilon_{\alpha_3}. \tag{17}$$

Here the energy of each nucleon in ^{3}He is one third of the energy of ^{3}He, namely,

$$\varepsilon_{\alpha_1} = \varepsilon_{\alpha_2} = \varepsilon_{\alpha_3} = \frac{\omega}{3}. \tag{18}$$

From the Dyson equation, the second-order term of the three-particle Green function can be also expressed as

$$\begin{aligned} & iG^{(2)}(\alpha_1\alpha_2\alpha_3, \beta_1\beta_2\beta_3; \omega) \\ & = -\frac{i}{\hbar} iG^{(0)}_{\alpha_1\alpha_2\alpha_3}(\omega) M^{(2)}(\alpha_1\alpha_2\alpha_3, \beta_1\beta_2\beta_3; \omega) iG^{(0)}_{\beta_1\beta_2\beta_3}(\omega). \end{aligned} \tag{19}$$

The second-order mass operator of the three-particle Green function can be obtained by comparing Eq. (16) with Eq. (19):

$$\begin{aligned} & M^{(2)}_{\alpha_1\alpha_2\alpha_3}(E) \\ & = \frac{1}{2} \sum_{\rho\delta\lambda} \frac{V_{\alpha_1\lambda,\delta\rho} V_{\delta\rho,\alpha_1\lambda}}{\varepsilon_{\alpha_1} - \varepsilon_\rho - \varepsilon_\delta + \varepsilon_\lambda + i\eta} n_\lambda (1-n_\delta)(1-n_\rho) \\ & \quad + \frac{1}{2} \sum_{\rho\delta\lambda} \frac{V_{\alpha_2\lambda,\delta\rho} V_{\delta\rho,\alpha_2\lambda}}{\varepsilon_{\alpha_2} - \varepsilon_\rho - \varepsilon_\delta + \varepsilon_\lambda + i\eta} n_\lambda (1-n_\delta)(1-n_\rho) \\ & \quad + \frac{1}{2} \sum_{\rho\delta\lambda} \frac{V_{\alpha_3\lambda,\delta\rho} V_{\delta\rho,\alpha_3\lambda}}{\varepsilon_{\alpha_3} - \varepsilon_\rho - \varepsilon_\delta + \varepsilon_\lambda + i\eta} n_\lambda (1-n_\delta)(1-n_\rho) \\ & = M^{(2)}_{\alpha_1}\left(\frac{E}{3}\right) + M^{(2)}_{\alpha_2}\left(\frac{E}{3}\right) + M^{(2)}_{\alpha_3}\left(\frac{E}{3}\right). \end{aligned} \tag{20}$$

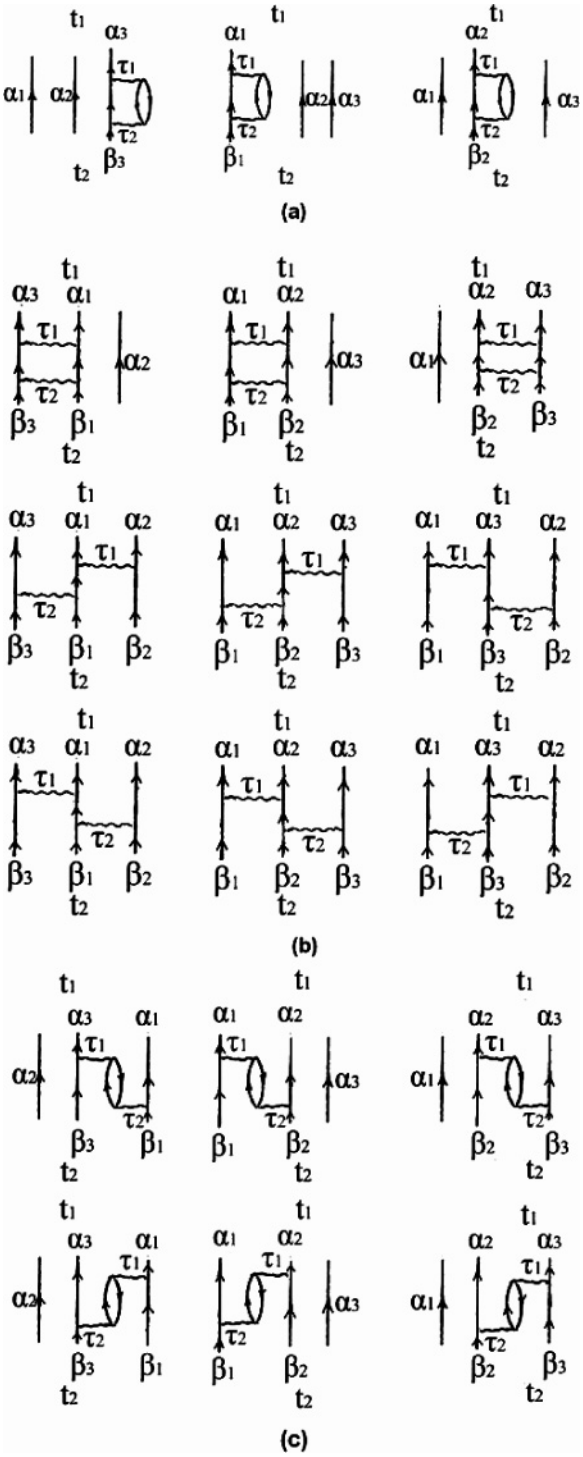

FIG. 2. The residual second-order Feynman diagrams of the three-particle Green function.

The imaginary part of the second-order mass operator $M^{(2)}_{\alpha_1\alpha_2\alpha_3}(E)$ is considered as the imaginary part of the microscopic optical potential for ^{3}He. According to the formula of the principal value integral

$$\frac{1}{x+i\eta} = P\left(\frac{1}{x}\right) - i\pi\delta(x), \tag{21}$$

the imaginary part of the MOP for ^{3}He can be obtained as follows:

$$\begin{aligned} W = \mathrm{Im}\, M^{(2)}_{\alpha_1\alpha_2\alpha_3}(E) &= -\frac{\pi}{2}\sum_{\rho\delta\lambda} V_{\alpha_1\lambda,\delta\rho} V_{\delta\rho,\alpha_1\lambda} n_\lambda (1-n_\delta) \\ &\times (1-n_\rho)\delta(\varepsilon_{\alpha_1} - \varepsilon_\rho - \varepsilon_\delta + \varepsilon_\lambda) \\ &- \frac{\pi}{2}\sum_{\rho\delta\lambda} V_{\alpha_2\lambda,\delta\rho} V_{\delta\rho,\alpha_2\lambda} n_\lambda (1-n_\delta)(1-n_\rho) \\ &\times \delta(\varepsilon_{\alpha_2} - \varepsilon_\rho - \varepsilon_\delta + \varepsilon_\lambda) \\ &- \frac{\pi}{2}\sum_{\rho\delta\lambda} V_{\alpha_3\lambda,\delta\rho} V_{\delta\rho,\alpha_3\lambda} n_\lambda (1-n_\delta)(1-n_\rho) \\ &\times \delta(\varepsilon_{\alpha_3} - \varepsilon_\rho - \varepsilon_\delta + \varepsilon_\lambda) \\ &= \mathrm{Im}\, M^{(2)}_{\alpha_1}\left(\frac{E}{3}\right) + \mathrm{Im}\, M^{(2)}_{\alpha_2}\left(\frac{E}{3}\right) + \mathrm{Im}\, M^{(2)}_{\alpha_3}\left(\frac{E}{3}\right), \end{aligned} \tag{22}$$

where $\mathrm{Im}\, M^{(2)}_{\alpha_1}(\frac{E}{3})$, $\mathrm{Im}\, M^{(2)}_{\alpha_2}(\frac{E}{3})$, and $\mathrm{Im}\, M^{(2)}_{\alpha_3}(\frac{E}{3})$ are the contributions of the imaginary parts of the MOP for the three nucleons [1,2] in ^{3}He, respectively.

An important conclusion can be gained from Eqs. (15) and (22) that, as the indirect interactions of the three nucleons in ^{3}He is ignored, the helium-3 microscopic optical potential is the sum of the microscopic optical potentials for its constituent nucleons.

Since the extended Skyrme force, which is density-dependent two-body interaction, is applied widely and successful in many aspects, it is adopt to express the two-body interaction in Eq. (11). There are many sets of Skyrme interactions, but they can be expressed in a unified form as

$$\begin{aligned} V_{12}(\vec{R},\vec{r}) &= t_0(1+x_0P_\sigma)\delta(\vec{r}) + \tfrac{1}{6}t_3(1+x_3P_\sigma)\rho^\alpha(\vec{R})\delta(\vec{r}) \\ &+ \tfrac{1}{2}t_1(1+x_1P_\sigma)(\vec{k'}^2\delta(\vec{r}) + \delta(\vec{r})\vec{k}^2) \\ &+ \tfrac{1}{2}t_4(1+x_4P_\sigma)(\vec{k'}^2\rho(\vec{R})\delta(\vec{r}) + \delta(\vec{r})\rho(\vec{R})\vec{k}^2) \\ &+ t_2(1+x_2P_\sigma)\vec{k'}\cdot\delta(\vec{r})\vec{k} \\ &+ t_5(1+x_5P_\sigma)\vec{k'}\cdot\rho(\vec{R})\delta(\vec{r})\vec{k} \\ &+ iW_0(\vec{\sigma}_1+\vec{\sigma}_2)\cdot\vec{k'}\times\delta(\vec{r})\vec{k}, \end{aligned} \tag{23}$$

where

$$\vec{r} = \vec{r}_1 - \vec{r}_2, \quad \vec{R} = \tfrac{1}{2}(\overrightarrow{r_1} + \overrightarrow{r_2}) \tag{24}$$

and the relative momentum operators

$$\vec{k} = \frac{1}{2i}(\vec{\nabla}_1 - \vec{\nabla}_2) \tag{25}$$

acting on the wave function on the right and

$$\vec{k'} = -\frac{1}{2i}(\vec{\nabla}_1 - \vec{\nabla}_2) \tag{26}$$

acting on the wave function on the left. The quantities P_σ and σ_i represent the spin exchange operator and the Pauli spin matrices, respectively.

TABLE I. Extended Skyrme force GS2 parameters.

	t_0 MeV · fm^3	t_1 MeV · fm^5	t_2 MeV · fm^5	t_3	t_4 MeV · fm^8	t_5 MeV · fm^8	α
GS2	−1177	670	−49.7	11054	−775	0	1
	W_0 MeV · fm^5	x_0	x_1	x_2	x_3	x_4	x_5
GS2	105	0.124	0	0	1	1	0

It is shown [2] that the nucleon microscopic optical potential obtained from the extended Skyrme interaction GS2 is more reasonable than those obtained from other Skyrme forces. In this paper GS2, the parameters of which are listed in Table I, is used.

In the nuclear matter, the wave function of nucleon α in Eq. (11) is given by the plane wave

$$\psi_\alpha(\vec{r}) = \frac{1}{\sqrt{\Omega}} e^{i\vec{k}_\alpha\cdot\vec{r}}\chi_{\sigma_\alpha}\chi_{\tau_\alpha}, \tag{27}$$

where χ_{σ_α} and χ_{τ_α} are the spin and isospin wave functions, respectively, and Ω is the volume.

When the distribution of the protons and neutron in ^{3}He is considered, the MOP for ^{3}He can be obtained by folding [10] the microscopic optical potentials of its constituent nucleons in the ground state of helium-3. In the relative coordinate representation, the microscopic optical potential for ^{3}He can be expressed as

$$\begin{aligned} V_{\mathrm{He3}}(\vec{R}) = \int\int |\psi(\vec{\xi}_1,\vec{\xi}_2)|^2 \Bigg[& V_n\left(\vec{R}+\frac{1}{3}\vec{\xi}_2+\frac{1}{2}\vec{\xi}_1\right) \\ & + V_p\left(\vec{R}+\frac{1}{3}\vec{\xi}_2-\frac{1}{2}\vec{\xi}_1\right) \\ & + V_p\left(\vec{R}-\frac{2}{3}\vec{\xi}_2\right)\Bigg] d\vec{\xi}_1\, d\vec{\xi}_2, \end{aligned} \tag{28}$$

where

$$\begin{cases} \vec{R} = \frac{1}{3}(\vec{r}_1+\vec{r}_2+\vec{r}_3) \\ \vec{\xi}_1 = \vec{r}_1-\vec{r}_2 \\ \vec{\xi}_2 = \frac{1}{2}(\vec{r}_1+\vec{r}_2)-\vec{r}_3 \end{cases} \tag{29}$$

with $\vec{r}_1, \vec{r}_2, \vec{r}_3$ indicating the position of the nucleons in ^{3}He and $\vec{R}$ indicating the position of the centroid of ^{3}He. V_n and V_p are the microscopic optical potentials for the neutron and the protons in ^{3}He, respectively, and the energy of each nucleon in ^{3}He is one-third of the incident helium-3 energy. The expressions of V_n and V_p are given in Ref. [1]. $\psi(\vec{\xi}_1,\vec{\xi}_2)$ is the ground state wave function of ^{3}He, which is given by the wave function of three-dimensional harmonic oscillator,

$$\psi(\vec{\xi}_1,\vec{\xi}_2) = \left(\frac{\beta^2}{3\pi^2}\right)^{\frac{3}{4}} e^{-\frac{1}{4}\beta\xi_1^2-\frac{1}{3}\beta\xi_2^2}, \tag{30}$$

where

$$\beta = \frac{1}{1.88^2}. \tag{31}$$

Then the microscopic optical potential for ^{3}He can be expressed as

$$\begin{aligned} V(R) = (2\pi)^2 \int \Bigg[& \left(\frac{\beta^2}{3\pi^2}\right)^{\frac{3}{4}} e^{-\frac{1}{4}\beta\xi_1^2-\frac{1}{3}\beta\xi_2^2}\Bigg]^2 \\ & \times \Bigg[V_n\Bigg(\Bigg(R^2+\frac{1}{9}\xi_2^2+\frac{2}{3}R\xi_2\mu_2+\frac{1}{4}\xi_1^2 \\ & + \left(R^2+\frac{1}{9}\xi_2^2+\frac{2}{3}R\xi_2\mu_2\right)^{\frac{1}{2}}\xi_1\mu_1\Bigg)^{\frac{1}{2}}\Bigg) \\ & + V_p\Bigg(\Bigg(R^2+\frac{1}{9}\xi_2^2+\frac{2}{3}R\xi_2\mu_2+\frac{1}{4}\xi_1^2 \\ & - \left(R^2+\frac{1}{9}\xi_2^2+\frac{2}{3}R\xi_2\mu_2\right)^{\frac{1}{2}}\xi_1\mu_1\Bigg)^{\frac{1}{2}}\Bigg) \\ & + V_p\Bigg(\left(R^2+\frac{4}{9}\xi_2^2-\frac{4}{3}R\xi_2\mu_2\right)^{\frac{1}{2}}\Bigg)\Bigg] \\ & \times \xi_1^2\xi_2^2 d\xi_1 d\mu_1 d\xi_2 d\mu_2, \end{aligned} \tag{32}$$

where $-1 \leqslant \mu_1 \leqslant 1$, $-1 \leqslant \mu_2 \leqslant 1$.

The local density approximation [11,12] is used to obtain the MOP for finite nuclei as in Refs. [1,2], and the densities of the neutrons and protons in a spherical nucleus are expressed by Negele's empirical formula [11]:

$$\rho_k(r) = \frac{\rho_{0k}}{1+\exp[(r-c)/a]}, \quad k = N \text{ or } Z, \tag{33}$$

where

$$\rho_{0k} = \frac{3k}{4\pi c^3(1+\pi^2a^2/c^2)}, \tag{34}$$

$$c = \left(0.978+0.0206A^{\frac{1}{3}}\right)A^{\frac{1}{3}}, \quad a = 0.54. \tag{35}$$

The spin-orbit couple potential for ^{3}He is considered as the sum of the spin-orbit couple potentials for its constituent nucleons:

$$V_{\mathrm{SO}}(r) = V_{\mathrm{SO}}^n + V_{\mathrm{SO}}^{p_1} + V_{\mathrm{SO}}^{p_2}, \tag{36}$$

where V_{SO}^n, $V_{\mathrm{SO}}^{p_1}$, and $V_{\mathrm{SO}}^{p_2}$ are the nucleon spin-orbit potentials which are obtained in Refs. [2,13].

III. CALCULATED RESULTS AND ANALYSIS

The radial dependence, the volume integral per nucleon, and the root mean square (rms) radii of the helium-3 microscopic optical potential are calculated. And the reaction cross sections and elastic scattering angular distributions are also calculated

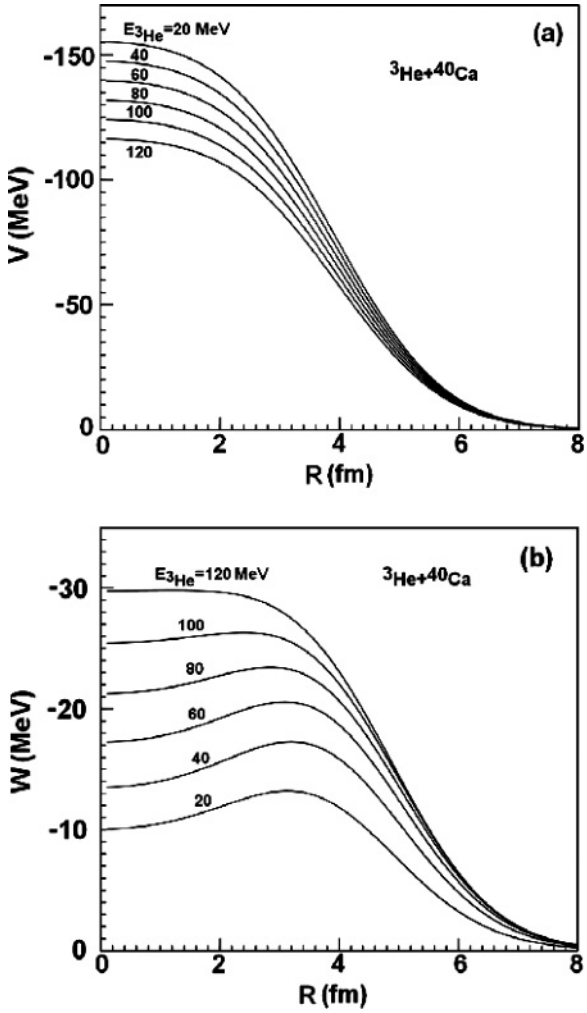

FIG. 3. Radial dependence of ^{3}He MOP for ^{40}Ca. (a) The real parts. (b) The imaginary parts.

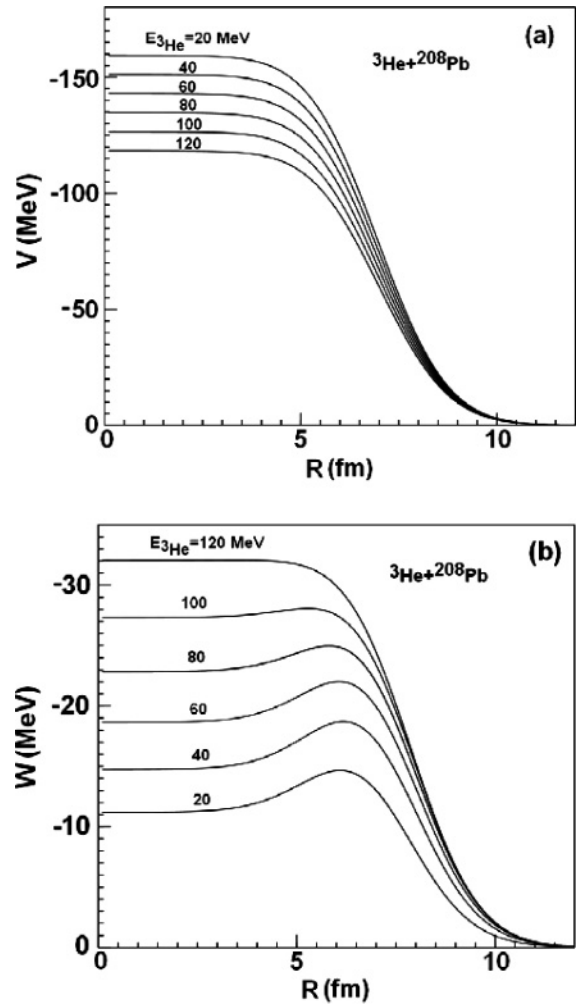

FIG. 4. Radial dependence of ^{3}He MOP for ^{208}Pb. (a) The real parts. (b) The imaginary parts.

by the MOP for nuclides in the mass range $12 \leqslant A \leqslant 208$ with incident energies from threshold up to 200 MeV.

The radial dependence of the real and imaginary parts of the helium-3 microscopic optical potential for ^{40}Ca and ^{208}Pb at incident energies from 20 to 120 MeV is shown in Figs. 3 and 4. In Figs. 3(a) and 4(a), the absolute value of the real part decreases with increasing radius and incident energy. In Figs. 3(b) and 4(b), the absolute value of the imaginary part increases with increasing incident energy, and the contribution of the imaginary part of the MOP changes from the dominant surface absorption into the volume absorption as the incident energy increases. For the same incident energy, the contribution of the volume absorption of the imaginary part increases with increasing mass number of the target nucleus.

The volume integral per nucleon of the MOP for ^{3}He is expressed as

$$J_V = -\frac{1}{A_{\mathrm{He3}} A_T} \int V(r) d\vec{r}, \qquad J_W = -\frac{1}{A_{\mathrm{He3}} A_T} \int W(r) d\vec{r} \tag{37}$$

and the rms radii is expressed as

$$\langle R_V^2 \rangle^{1/2} = \left[\frac{\int V(r) r^2 d\vec{r}}{\int V(r) d\vec{r}} \right]^{1/2}, \qquad \langle R_W^2 \rangle^{1/2} = \left[\frac{\int W(r) r^2 d\vec{r}}{\int W(r) d\vec{r}} \right]^{1/2} \tag{38}$$

The energy dependence of the volume integral per nucleon and the rms radii for ^{12}C, ^{27}Al, ^{40}Ca, ^{58}Ni, ^{116}Sn, and ^{208}Pb is shown in Figs. 5 and 6.

Figure 5 shows the volume integral per nucleon of the real and imaginary parts of the MOP decreases with increasing mass number, and the volume integral per nucleon of the real part J_V is linearly dependent on the incident energy and decreases as the incident energy increases, while the volume integral per nucleon of the imaginary part J_W increases with increasing energy.

As shown in Fig. 6, the rms radii of the real and imaginary parts of the MOP increase when the mass number increases, and keep basically as a constant.

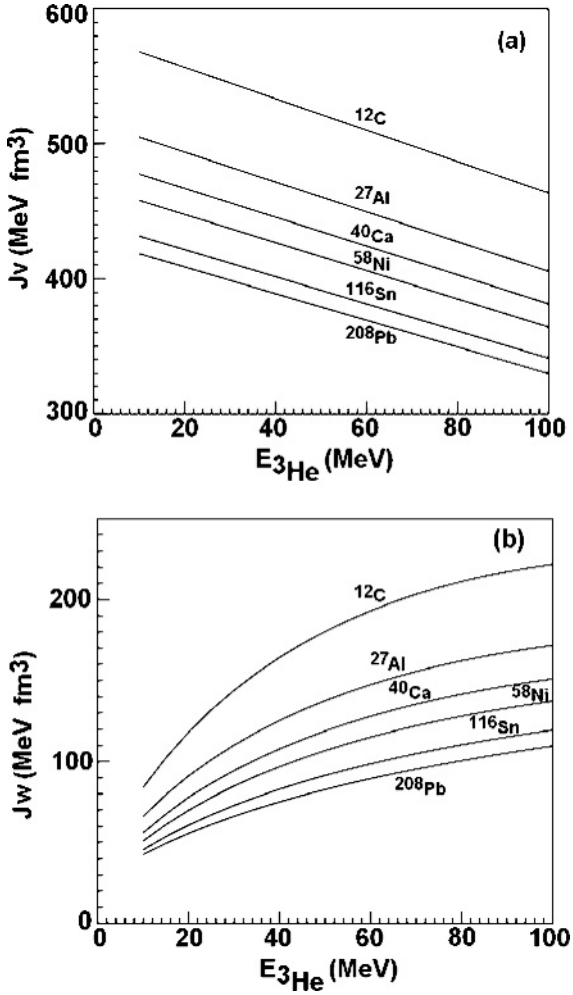

FIG. 5. The volume integral per nucleon of ^{3}He MOP for different nuclei against the incident energy $E_{^3\mathrm{He}}$. (a) The real parts. (b) The imaginary parts.

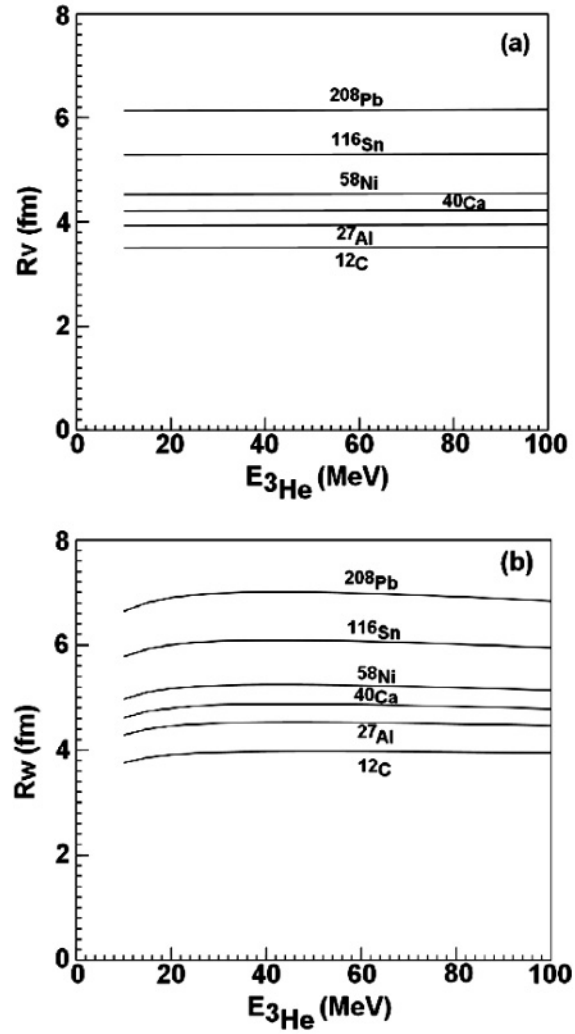

FIG. 6. The root mean square radii of MOP for ^{3}He scattering by different nuclei against ^{3}He energy. (a) The real parts. (b) The imaginary parts.

The comparisons between the calculated results of ^{3}He reaction cross sections and the experimental data [14] for ^{12}C, ^{16}O, ^{28}Si, ^{40}Ca, ^{58}Ni, ^{60}Ni, ^{112}Sn, ^{116}Sn, ^{118}Sn, ^{120}Sn, ^{124}Sn, and ^{208}Pb are given in Fig. 7. It is shown that the shape of the calculated results curve of reaction cross sections for ^{12}C and ^{16}O are similar to the experimental data, while the magnitudes are larger than those of experimental data. The calculated results for ^{28}Si, ^{40}Ca, ^{58}Ni, ^{60}Ni, ^{112}Sn, ^{116}Sn, ^{118}Sn, ^{120}Sn, ^{124}Sn, and ^{208}Pb are in agreement with the experimental data. Figure 7 also shows there is a general trend that the reaction cross sections increase with increasing mass number of the target nucleus and that the reaction cross sections for heavy nuclei increase with increasing incident energy from threshold up to 200 MeV, while for light nuclei the reaction cross sections increase first, and then decrease with increasing incident energy.

The elastic scattering angular distributions of ^{3}He from natural targets C, Mg, Al, Si, Ca, Y, and In as well as ^{56}Fe and ^{63}Cu at incident energy of 29 MeV were measured [4]. The calculated results of elastic scattering angular distributions for ^{12}C, ^{24}Mg, ^{27}Al, ^{28}Si, ^{40}Ca, ^{89}Y, and ^{115}In corresponding to natural targets as well as for ^{56}Fe and ^{63}Cu are compared with the experimental data in Fig. 8. It is shown that the calculated results for ^{12}C, ^{24}Mg, ^{27}Al, ^{28}Si, and ^{40}Ca are in reasonable agreement with the experimental data for angles less than 50°, while larger than the experimental data for angles greater than 50°, where the curve shapes of present calculated results, however, are similar to ones of experimental data. The reason for the disagreement is light nuclei have a certain nuclear structure effect, and the nuclear structure effect may be strong at low energy. For ^{56}Fe, ^{63}Cu, ^{89}Y, and ^{115}In, the calculated results are in good agreement with the experimental data.

The experimental data of differential cross sections relative to Rutherford cross sections for elastic scattering of ^{3}He from ^{40}Ca, ^{58}Ni, ^{90}Zr, and ^{116}Sn at incident energy of 109.2 MeV were given in Ref. [15]. The comparison between the calculated results from the MOP and the experimental data is shown in Fig. 9. The figure shows the calculated results for ^{40}Ca, ^{58}Ni, ^{90}Zr, and ^{116}Sn are in good agreement with the experimental data for the angle smaller than 50°. For the angle

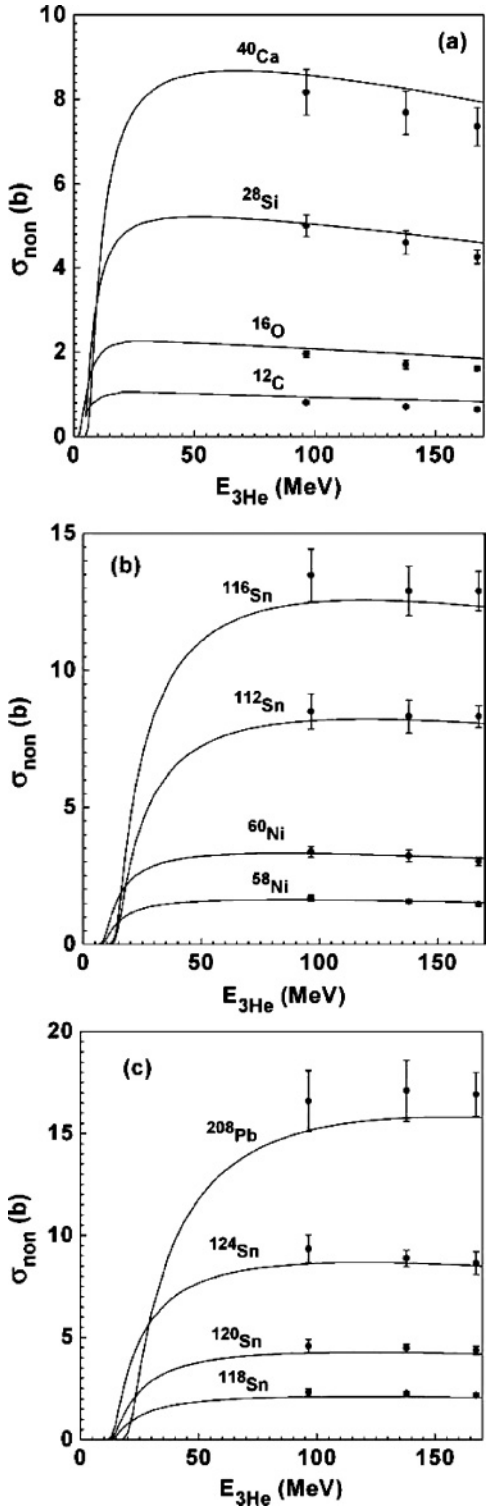

FIG. 7. Comparison of the theoretical values (solid line) of the ^{3}He reaction cross section for different nuclei with experimental data (symbols) [14]. Different data sets are offset by factors of 2, 4, 6.

greater than 50°, however, the magnitudes of the calculated results are larger than those of the experimental data.

The calculated results from the MOP are also compared with the experimental data [16] of differential cross sections

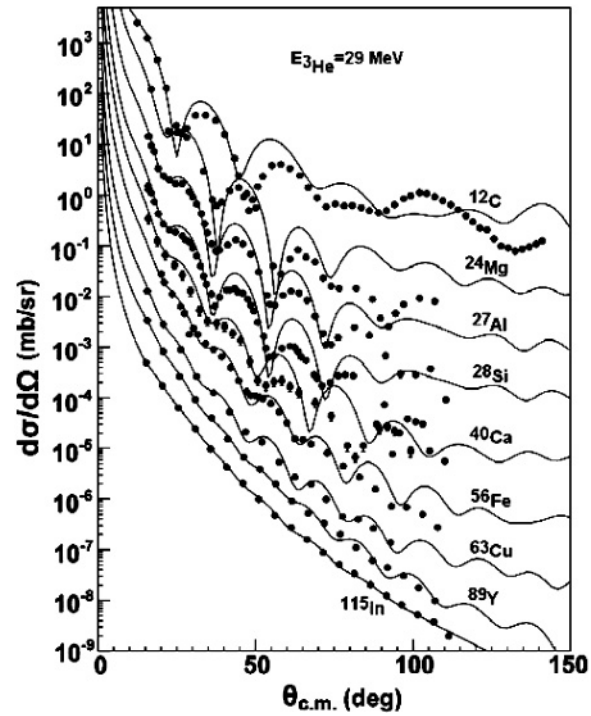

FIG. 8. Comparison of the theoretical values (solid line) of the ^{3}He elastic scattering angular distribution for different nuclei at incident ^{3}He energy of 29 MeV with experiment data (symbols) [4]. The results are offset by factors of 10.

relative to Rutherford cross sections for the elastic scattering of 119 MeV ^{3}He from ^{12}C, ^{27}Al, ^{59}Co, ^{58,60,62,64}Ni, ^{89}Y, ^{90,92}Zr in Fig. 10. The comparison shows that a very good agreement is obtained for every nuclide for the angle smaller than 50°, and

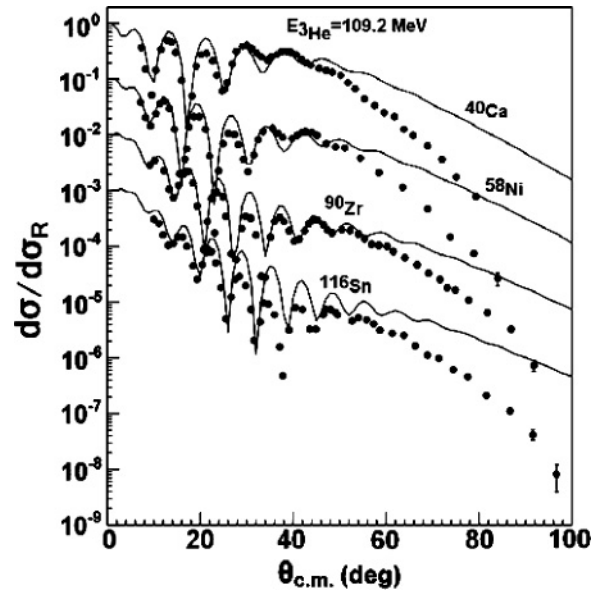

FIG. 9. Calculated elastic scattering angular distributions in the Rutherford ratio (solid line) at incident ^{3}He energy of 109.2 MeV for different nuclei compared with experimental data (symbols) [15]. The results are offset by factors of 10.

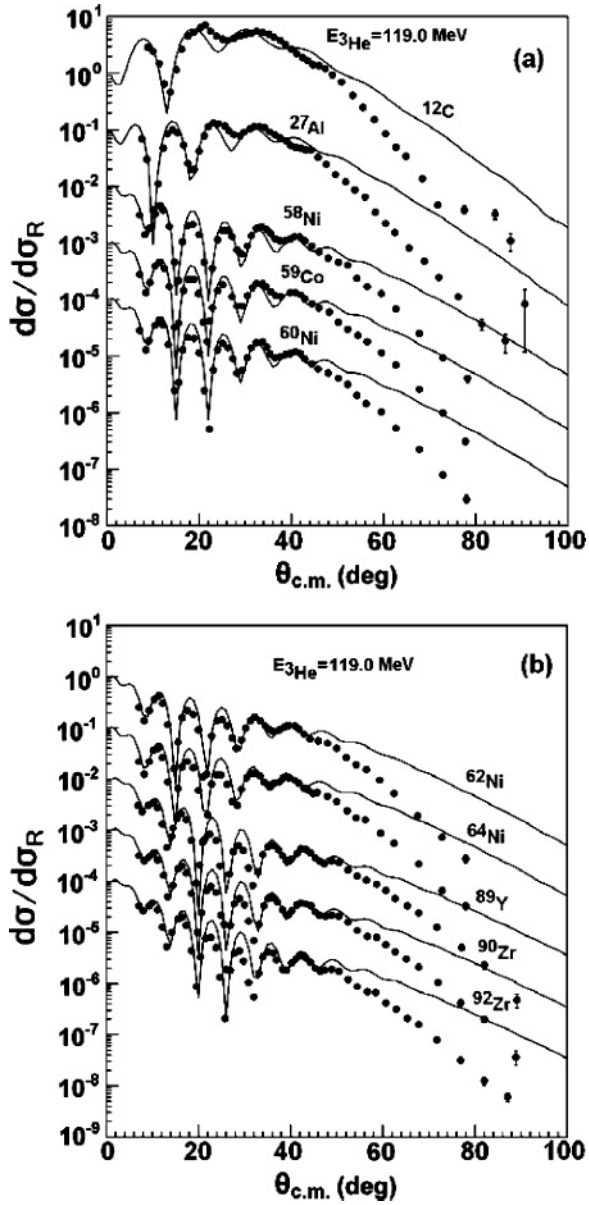

FIG. 10. Calculated elastic scattering angular distributions in the Rutherford ratio (solid line) at incident ^{3}He energy of 119.0 MeV for different nuclei compared with experimental data (symbols) [16]. The results are offset by factors of 10.

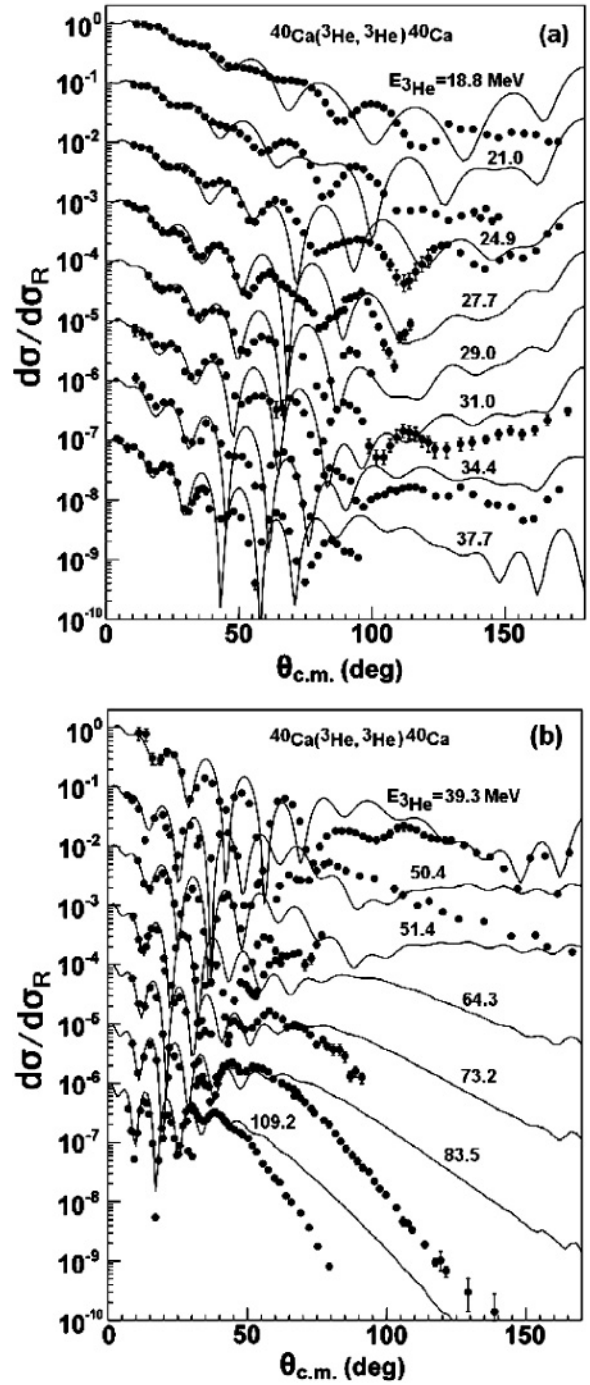

FIG. 11. Calculated elastic scattering angular distributions in the Rutherford ratio (solid line) at different incident ^{3}He energy compared with experimental data (symbols) [4,5,15,17–20] for ^{3}He + ^{40}Ca reaction. The results are offset by factors of 10.

for the angle greater than 50°, the magnitudes of the calculated results are larger than those of the experimental data.

The calculated results of the differential cross sections relative to Rutherford cross sections for same target nucleus at different incident ^{3}He energies are compared with experimental data. The comparison between the calculated results and experimental data [4,5,15,17–20] for ^{40}Ca at incident energies from 18.8 to 109.2 MeV is given in Fig. 11. The present calculated results are in good agreement with experimental data for all energy points as the angle less than 50°. For the larger degrees, the shapes of present calculated results curve are similar to those of the experimental data, but the values are inconsistent with the experimental data.

The calculated results of the differential cross sections relative to Rutherford cross sections for ^{58}Ni at incident energies from 21.9 to 119.0 MeV are compared with the experimental data [5,15,16,18,21–23] in Fig. 12. The calculated results are in good agreement with the experimental data for the angle less than 50°. For the larger degrees, the shapes of present calculated results curve are similar to

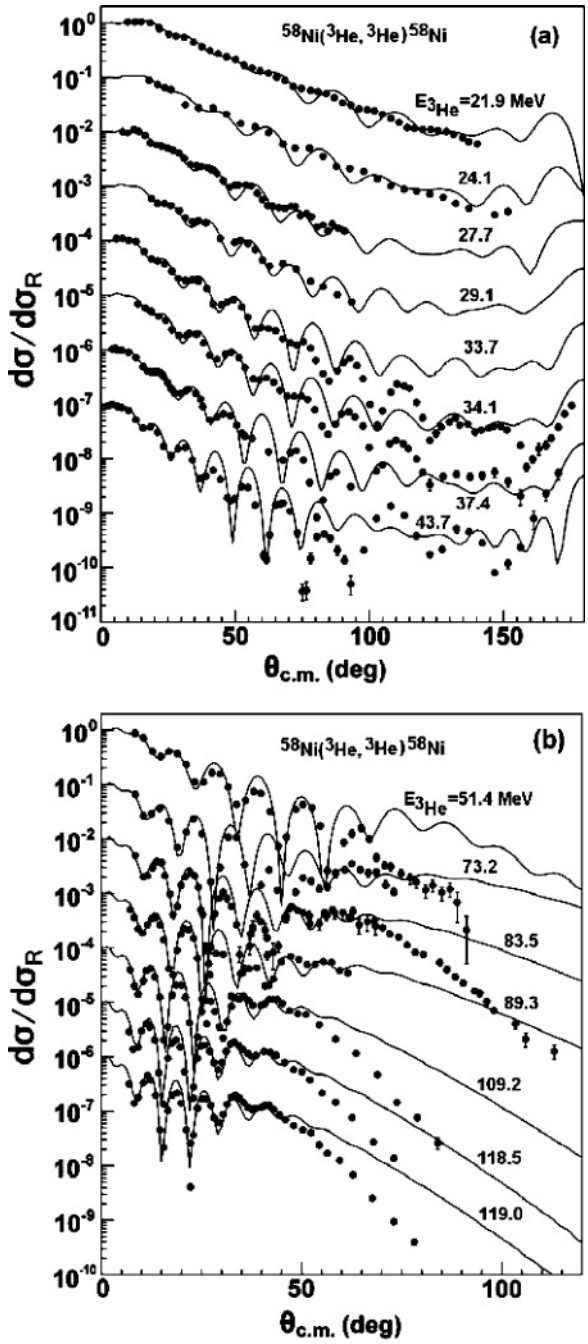

FIG. 12. Calculated elastic scattering angular distributions in the Rutherford ratio (solid line) at different incident ^{3}He energy compared with experimental data (symbols) [5,15,16,18,21–23] for $^3\mathrm{He} + {}^{58}\mathrm{Ni}$ reaction. The results are offset by factors of 10.

ones of experimental data, but the magnitudes are larger than those of the experimental data at the incident energies above 83.5 MeV.

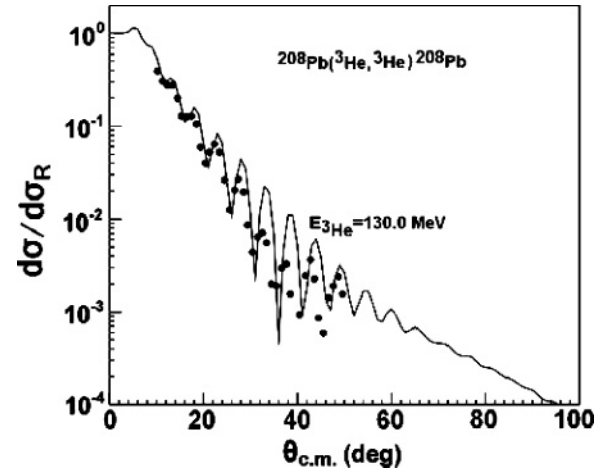

FIG. 13. Calculated elastic scattering angular distributions in the Rutherford ratio (solid line) at incident ^{3}He energy of 130 MeV compared with experimental data (symbols) [24] for $^3\mathrm{He} + {}^{208}\mathrm{Pb}$ reaction.

The calculated results of differential cross sections relative to Rutherford cross sections for the elastic scattering of 130 MeV ^{3}He from ^{208}Pb are compared with experimental data [24] in Fig. 13. The calculated results are in reasonable agreement with the experimental data.

IV. SUMMARY

The helium-3 microscopic optical potential is obtained by Green function method. The radial dependence, the volume integral per nucleon and the root mean square (rms) radii of the helium-3 microscopic optical potential are calculated. The reaction cross sections and elastic scattering angular distributions for nuclides in the mass range $12 \leqslant A \leqslant 208$ with incident energies from threshold up to 200 MeV are calculated by the helium-3 microscopic optical potential, and the calculated results are compared with the experimental data. Good agreement is generally obtained for the reaction cross sections, and in most cases, the calculated elastic scattering angular distributions are in reasonable agreement with experimental data.

ACKNOWLEDGMENTS

This work is one of the National Basic Research Program of China (973 Program), that is Key Technology Research of Accelerator Driven Sub-critical System for Nuclear waste Transmutation, and supported by the China Ministry of Science and Technology under Contract No. 2007CB209903.

[1] Shen Qingbiao, Zhang Jingshang, Tian Ye, Ma Zhongyu, and Zhuo Yizhong, Z. Phys. A **303**, 69 (1981).
[2] Zhuo Yizhong, Shen Qingbiao, and Tian Ye, Advance in Science of China, Physics **1**, 231 (1985) (in Chinese).
[3] C. S. Lu, J. S. Zhang, and Q. B. Shen, High Energy Phys. Nucl. Phys. **15**, 919 (1991) (in Chinese).
[4] D. J. Baugh, G. J. B. Pyle, P. M. Rolph, and S. M. Scarrott, Nucl. Phys. **A95**, 115 (1967).

[5] H. H. Chang and B. W. Ridley, Nucl. Phys. **A297**, 105 (1978).
[6] D. Y. Pang, P. Roussel-Chomaz, H. Savajols, R. L. Varner, and R. Wolski, Phys. Rev. C **79**, 024615 (2009).
[7] S. K. Samaddar and R. K. Satpathy, Nucl. Phys. **A150**, 655 (1970).
[8] Bikash Sinha, Feroze Duggan, and Richard J. Griffiths, Nucl. Phys. **A241**, 229 (1975).
[9] J. S. Bell and E. J. Squires, Phys. Rev. Lett. **3**, 96 (1959).
[10] F. G. Perey and G. R. Satchler, Nucl. Phys. **A97**, 515 (1967).
[11] J. W. Negele, Phys. Rev. C **1**, 1260 (1970).
[12] J. P. Jeukenne, A. Lejeune, and C. Mahaux, Phys. Rev. C **16**, 80 (1977).
[13] D. Vautherin and D. M. Brink, Phys. Rev. C **5**, 626 (1972).
[14] A. Ingemarsson, G. J. Arendse, A. Auce *et al.*, Nucl. Phys. **A696**, 3 (2001).
[15] M. Hyakutake, I. Kumabe *et al.*, Nucl. Phys. **A311**, 161 (1978).
[16] M. Hyakutake, I. Kumabe *et al.*, Nucl. Phys. **A333**, 1 (1980).
[17] N. Nakanishi, Y. Chiba, Y. Awaya, and K. Matsuda, Nucl. Phys. **A140**, 417 (1970).
[18] E. F. Gibson, B. W. Ridley, J. J. Kraushaar, M. E. Rickey, and R. H. Bassel, Phys. Rev. **155**, 1194 (1967).
[19] R. J. Griffiths, F. Duggan, and N. M. Clarke, J. Phys. G **7**, 381 (1981).
[20] A. Springer, M. Chabre, D. L. Hendrie, and H. G. Pugh, Phys. Lett. **20**, 397 (1966).
[21] P. D. Kunz, E. Rost *et al.*, Phys. Rev. **185**, 1528 (1969).
[22] M. E. Cage, D. L. Clough *et al.*, Nucl. Phys. **A183**, 449 (1972).
[23] P. P. Urone, L. W. Put, B. W. Ridley, and G. D. Jones, Nucl. Phys. **A167**, 383 (1971).
[24] A. Djaloeis, J. P. Didelez, A. Galonsky, and W. Oelert, Nucl. Phys. **A306**, 221 (1978).